ACS Catalysis

Research Article

pubs.acs.org/acscatalysis

Sorbent-Enhanced Methane Reforming over a Ni−Ca-Based, Bifunctional Catalyst Sorbent

Marcin Broda,[†] Agnieszka M. Kierzkowska,[†] David Baudouin,[‡] Qasim Imtiaz,[†] Christophe Copéret,[‡] and Christoph R. Müller[†,*]

[†]Laboratory of Energy Science and Engineering, Institute of Energy Technology, ETH Zurich, Leonhardstrasse 27, 8092 Zurich, Switzerland

[‡]Institute of Inorganic Chemistry, ETH Zurich, Wolfgang-Pauli-Strasse 10, 8093 Zurich, Switzerland

Supporting Information

ABSTRACT: A bifunctional catalyst for the sorbent-enhanced steam methane reforming (SE-SMR) reaction was derived from a hydrotalcite-based precursor synthesized via a coprecipitation technique. The material contained both the Ni reforming catalyst and the Ca-based CO_2 sorbent and was characterized using X-ray diffraction, H_2 chemisorption, N_2 physisorption, transmission electron microscopy, and temperature-programmed reduction. Reduction of the calcined hydrotalcite converted the $(Al:Ca:Mg:Ni)O_x$ mixed oxide into nickel and CaO particles supported on an $(Al:Mg)O_x$ matrix with a surface area of 54 $m^2 \cdot g^{-1}$. The high CO_2 absorption capacity and its stability with carbonation cycles was attributed to the high dispersion of CaO on the porous and thermally stable $(Al:Mg)O_x$ network, whereas for naturally occurring limestone, a rapid decay in the CO_2 absorption capacity was observed. Under SE-SMR conditions, the recorded mole fraction of hydrogen in the effluent stream was 99 vol % (dry and without inert component); that is, thermodynamic equilibrium calculated to be 99 vol % (without inert component) was reached. The CO_2 uptake of the bifunctional material averaged 0.074 g CO_2/g sorbent over 10 cycles. After approximately seven cycles, the CO_2 capture capacity stabilized, resulting in an average decay rate of only 0.3% per cycle over the last three cycles. The bifunctional material developed here produced a larger amount of high-purity H_2 than limestone mixed with Ni−SiO_2 or a Ca-free, nickel hydrotalcite-derived catalyst, making the new material an interesting candidate for the SE-SMR process.

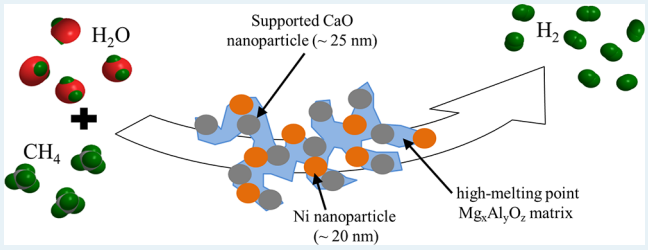

KEYWORDS: *sorbent-enhanced steam methane reforming, bifunctional catalyst, CO_2 capture, hydrogen, nickel catalyst, calcium oxide*

1. INTRODUCTION

The use of hydrogen as an energy carrier is seen as a possibility for mitigating climate change arising from the anthropogenic emission of CO_2 into the atmosphere. For example, hydrogen produced via the large-scale decarbonization of a hydrocarbonaceous fuel could allow decarbonization of the transportation sector by using hydrogen-powered fuel cell technology; however, for hydrogen to fulfill its potential as a clean energy carrier, it must be produced in a sustainable manner, for example, from renewable resources, such as woody biomass. Alternatively, if hydrogen is to be derived from a fossil fuel, it has to be produced with simultaneous capture and subsequent storage or conversion of the CO_2.

The currently dominating process for the production of H_2 is steam methane reforming, a highly endothermic process that releases a large amount of CO_2 into the atmosphere. In a hydrogen production plant employing the steam methane reforming process, the methane steam reforming reaction, namely,

$$CH_4 + H_2O \leftrightarrow CO + 3H_2 \qquad \Delta H^0_{25\,^\circ C} = 206\ \text{kJ/mol} \tag{1}$$

typically performed over a Ni catalyst, is the first step. Since the methane steam reforming reaction is highly endothermic, high reaction temperatures in the range of 850−1000 °C are employed to achieve high methane conversions.[1] The concentration of CO in the effluent gas of the steam reformer is ∼12 vol %;[2,3] therefore, to further convert CO to CO_2, high- (Fe/Cr catalyst) and low-temperature (Cu/Zn/Al catalyst) water gas shift (WGS) reactions,

$$CO + H_2O \leftrightarrow CO_2 + H_2 \qquad \Delta H^0_{25\,^\circ C} = -41\ \text{kJ/mol} \tag{2}$$

producing an equivalent of H_2, are employed. Since the water-gas-shift reaction is moderately exothermic, low operating conditions are favorable. The concentration of CO in the effluent of the water-gas-shift reactor is ∼0.5−1.0 vol %.[2,3] To further reduce the concentration of CO, an additional step, for example, preferential oxidation, is required.

Received: February 16, 2012
Revised: June 25, 2012
Published: June 26, 2012

To reduce the operational complexity and the severeness of the operating conditions, an alternative approach for the production of high-purity hydrogen, the so-called sorbent-enhanced steam methane reforming (SE-SMR) reaction has been proposed.[4] In this process, the steam reforming of methane (eq 1) is run simultaneously with the water-gas-shift reaction 2 and a CO_2 abstraction reaction, for example, the carbonation reaction of CaO 3:

$$CO_2 + CaO \leftrightarrow CaCO_3 \qquad \Delta H^0_{25^\circ C} = -178\ \text{kJ/mol} \tag{3}$$

The summation of reactions 1-3 gives

$$CH_4 + 2H_2O + CaO \leftrightarrow CaCO_3 + 4H_2 \qquad \Delta H^0_{25^\circ C} = -13\ \text{kJ/mol} \tag{4}$$

with the thermodynamic equilibrium at operating temperatures of <575 °C being almost completely on the product side, thus producing high-purity hydrogen. Equilibrium thermodynamics predict the formation of $Ca(OH)_2$ for temperatures <600 °C, resulting in lower hydrogen yields;[5] however, the hydrogen yields obtained from measurements in a packed bed reactor showed only a small decrease in the hydrogen yield with decreasing temperature, indicating that $Ca(OH)_2$ formed only to a small extent in the temperature range investigated (T = 500−600 °C).[4] With regard to the CO_2 capture capacity of CaO-based sorbents, a slight improvement in the cyclic CO_2 uptake was observed under wet conditions.[6] This observation was attributed to an enhanced diffusive transport of CO_2 through the $CaCO_3$ product layer under wet conditions.[6]

An important advantage of the SE-SMR reaction is the possibility to be operated at lower temperature, thus reducing catalyst deactivation due to sintering and coking.[7,8] In addition, a decrease in the investment and operational costs of a hydrogen plant may be feasible, since (i) the water gas shift and further hydrogen purification steps may be omitted and (ii) the size of the heat exchangers can be significantly reduced.[3]

After the carbonation of CaO, the $CaCO_3$ formed is regenerated at elevated temperatures through the reverse of eq 3, yielding a pure stream of CO_2 suitable for further conversion or sequestration, for example, in saline aquifers. Arguably, the two cornerstones of the SE-SMR process are the development of (i) catalysts that are highly active at the low reforming temperatures and stable at the regeneration temperatures and (ii) sorbents that possess high and stable, cyclic CO_2 uptakes. Hydrotalcites have previously been considered as candidates for use as CO_2 sorbents in the SE-SMR reaction.[8]

Reijers et al.[8] determined a CO_2 capture capacity of potassium promoted hydrotalcite of ∼0.009 g CO_2/g sorbent at 400 °C that reduced to 0.004 g CO_2/g sorbent at 500 °C. Owing to the low CO_2 capture capacities of hydrotalcites at high operating temperatures, Reijers et al.[8] argued that hydrotalcites may be suitable for the sorbent-enhanced water-gas-shift reaction; however, owing to the higher operating temperatures, the SE-SMR reaction requires alternative, high-temperature CO_2 sorbents. Recently, Ochoa-Fernández et al.[9] reported a detailed thermodynamic analysis of the SE-SMR process, highlighting the importance of the CO_2 capture characteristics of the carbon dioxide sorbent on the hydrogen yield. It was concluded that none of the CO_2 sorbents investigated (CaO, Li_2ZrO_3, $KLiZrO_3$, Li_4SiO_4, Na_2ZrO_3) fulfilled all requirements regarding (i) CO_2 absorption capacity, (ii) capture stability, (iii) kinetics, (iv) regeneration temperature, and (v) thermodynamics, i.e. equilibrium partial pressure of CO_2 as a function of operating temperature.

Turning now to the thermal efficiency of the SE-SMR process, the thermal efficiency of a conventional, modern SMR unit is ∼86−88%;[9,10] however, the thermal efficiency reduces to 71% if CO_2 is removed from the hydrogen using pressure swing adsorption.[9] On the other hand, Ochoa-Fernández et al.[9] determined a substantially higher thermal efficiency of 82% for the SE-SMR process using CaO as the CO_2 sorbent. For the case that Li_2ZrO_3 was used as the CO_2 sorbent, the thermal efficiency was only 72%; that is, comparable to the standard SMR process with CO_2 removal. The favorable characteristics of CaO are due to its ability to react with CO_2 at lower CO_2 partial pressures and the lower steam-to-carbon ratio thaqt is required to yield a high methane conversion.[9] The process analysis performed by Ochoa-Fernández et al.[9] assumed that thermodynamic equilibrium was achieved. Therefore, to evaluate the economic feasibility of the SE-SMR process in more detail, technoeconomic studies, including also kinetic effects and the cyclic CO_2 uptake characteristics of the CO_2 sorbent, are required.

The favorable CO_2 capture characteristics of Ca-based, high-temperature CO_2 sorbents are in agreement with other reports (e.g., Solieman et al.[11] and Choi et al.[12]). CaO can be obtained most easily by calcination of naturally occurring $CaCO_3$ (e.g., limestone). Satorio et al.[13] developed a Ni−Ca-based material by pelletizing finely ground limestone or dolomite powders. The pellets were coated with an alumina shell and subsequently impregnated with a nickel nitrate solution. The developed material showed promising methane conversions, resulting in a mole fraction of H_2 in the range of 94−96 mol % when tested in a packed bed reactor in the temperature range of 520−650 °C. However, only three cycles of the SE-SMR reaction (at different temperatures) were performed, making an assessment of the stability of the developed material difficult. On the other hand, Martavaltzi and Lemonidou[14] developed a Ca−Ni-based material by impregnating solutions of aluminum and nickel nitrate on CaO, with the final material containing 70 wt % CaO. Using a steam-to-methane ratio of 3.4 and an operating temperature of 650 °C, the mole fraction of H_2 was 90%; however, the SE-SMR reaction was performed for only a single cycle. Balasubramanian et al.,[4] using a mixture of commercial nickel catalyst and limestone, reported that the conversion of CH_4 decreased with cycle number owing to the decrease in CO_2 capture capacity of the natural sorbents.[5] The rapid decay of the cyclic CO_2 capture capacity of limestone is well documented and has been attributed to sintering due to the low Tammann temperature of $CaCO_3$ of 533 °C,[15] accompanied by severe, detrimental alterations in the pore structure.[16,17]

Thus, several strategies have been proposed recently to reduce the decay in CO_2 capture performance of naturally occurring materials, for example, using thermal pretreatment[18,19] or regeneration by hydration.[20,21] An alternative that has attracted considerable interest is the development of synthetic, Ca-based, CO_2 sorbents.[22−36]

In this work, we have used a one-pot synthesis route to develop a material that contains both the reforming catalyst based on Ni and the CO_2 sorbent; namely, CaO. The development of such a bifunctional material was driven by a desire to increase the heat and mass-transfer characteristics between the endothermic reforming and exothermic carbonation reactions. A synthesis route using a hydrotalcite precursor was used to ensure that Ni and CaO particles were

dx.doi.org/10.1021/cs300247g | ACS Catal. 2012, 2, 1635−1646

embedded in a thermally stable $Mg_xAl_yO_z$-based matrix. To assess the performance of the bifunctional material, it was compared to (i) a mixture of a commercial silica-supported Ni catalyst and limestone and (ii) a mixture of a CaO-free, nickel hydrotalcite-based catalyst[37] and limestone. The performance of the three materials studied is discussed in light of a detailed characterization of the materials and their evolution with SE-SMR cycles with a particular focus on CO_2 capture and carbon formation characteristics.

2. EXPERIMENTAL SECTION

2.1. Catalyst Preparation. A Ca−Ni-rich, bifunctional material derived from a hydrotalcite structure (Ca−Ni-ex-Htlc) was prepared via a coprecipitation technique using a modification of the original technique used by He et al.[37] First, appropriate amounts of $Ca(NO_3)_2{\cdot}4H_2O$, $Ni(NO_3)_2{\cdot}6H_2O$, $Mg(NO_3)_2{\cdot}6H_2O$, and $Al(NO_3)_3{\cdot}9H_2O$ were dissolved in 400 mL of water (reverse osmosis, 15 MΩ·cm). The molar ratio of Mg^{2+} to Al^{3+} was 2:1. Subsequently, a solution containing NaOH (24 g) and Na_2CO_3 (6 g) in 400 mL of water was fed dropwise into the nitrate solution under continuous stirring. After the complete addition of the basic solution, the pH of the mixture was adjusted to 8.6 using nitric acid. The mixture was subsequently heated to 80 °C and kept at this temperature for 16 h under total reflux conditions. The resulting precipitate was cooled, washed, and filtered with water. The material was dried overnight at 70 °C and calcined at 600 °C for 6 h in an air atmosphere using a heating rate of 5 °C/min. Finally, the material was calcined at 800 °C in a N_2 atmosphere. The mass fractions of CaO and Ni in the final material were 21 and 45 wt %, respectively. A Ca^{2+}-free, Ni catalyst derived from a hydrotalcite structure (Ni-ex-Htlc) was synthesized for comparison. The pH of the mixture was adjusted to 8.6 using NaOH. The catalyst contained 47 wt % of Ni. Finally, a commercially available Ni−SiO_2 catalyst (Sigma Aldrich) containing 52 wt % of Ni was used for comparison.

2.2. Characterization. Nitrogen isotherms of the reduced and reacted catalytic material where measured at −196 °C using a Belmini apparatus (BEL, Japan). Prior to the measurements, the reduced samples were slowly oxidized and degassed at 250 °C for 10 h. On the other hand, N_2 isotherms of the calcined materials and cycled limestone were determined using a NOVA 4000e (Quantachrome) analyzer. Each sample was degassed at 300 °C for at least 3 h before characterization. The models of Brunauer et al.[38] and Barrett et al.[39] were used to calculate the surface area and pore size distribution, respectively.

Chemisorption experiments were carried out in a BELSORB-max (BEL, Japan). Approximately 100 mg of catalyst was reduced in situ under a flow of 30 mL·min^{-1} of pure hydrogen (5.0) at 750 °C (550 °C for Ni−SiO_2) for 2 h using a ramp of 10 °C·min^{-1}. Subsequently, the sample was degassed at 350 °C for 3 h under dynamic vacuum (10^{-6} mbar). The chemisorption measurements were performed at 25 °C, and the equilibrium pressures were recorded when the pressure variation was below 0.03% per minute. The quantity of surface nickel was calculated from the adsorption at saturation derived using a Langmuir adsorption model and a H/Ni adsorption stoichiometry factor of 1.[40,41] The calculated dispersion refers to the molar ratio of surface Ni to bulk Ni. Estimation of the average Ni particle size was based on a truncated octahedron geometry and assuming a complete reduction of nickel.

The crystallinity of the materials was studied by powder X-ray diffraction on an AXS D8 Advance (Bruker). The X-ray diffractometer was equipped with a Lynxeye superspeed detector and operated at 40 mA and 40 kV. Each sample was scanned within the 2θ range of 10−80°. The step size was 0.01° with a time duration per step of 0.8 s.

Transmission electron micrographs were obtained with a Philips CM12 operated at 100 kV.

2.3. TGA Test. The cyclic CO_2 uptake and TPR measurements were performed in a thermogravimetric analyzer (TGA, Mettler Toledo TGA/DSC 1). To study repeated cycles of the carbonation and calcination reactions, a small amount (∼40 mg) of sorbent was placed in an alumina crucible and heated to 750 °C at a rate of 10 °C·min^{-1} under a N_2 flow of 20 mL·min^{-1}. In addition, a constant N_2 flow of 25 mL·min^{-1} was used as purge flow over the microbalance. Once the reaction temperature was stabilized, a CO_2 flow of 30 mL·min^{-1} was added to the N_2 flow. Carbonation was performed for 20 min. After the carbonation, the CO_2 flow was stopped for 20 min to calcine the sorbent. For each sorbent, the carbonation/calcination cycle was repeated 10 times. The molar conversion of CaO was calculated from the continuously monitored weight change. To study the cyclic CO_2 uptake of reduced Ca−Ni-ex-Htlc, the carbonation reaction was performed in a mixture of 20 mL·min^{-1} of 5 vol % H_2 in N_2 and 30 mL·min^{-1} CO_2. The calcination was performed in N_2 flowing at 20 mL·min^{-1}.

In a typical TPR measurement, a small amount of catalyst (∼50 mg) was placed in an alumina crucible and heated to 1000 °C at a rate of 10 °C·min^{-1} under a flow of 70 mL·min^{-1}of 5% H_2 in N_2. The consumption of H_2 was monitored using a thermal conductivity analyzer (ABB Caldos27).

The rate of carbon deposition was studied in a thermogravimetric analyzer (TGA, Mettler Toledo TGA/DSC 1). A small amount (∼10 mg) of catalyst was placed in an alumina crucible and heated to 750 °C (550 °C for Ni−SiO_2) at a rate of 10 °C·min^{-1} under a N_2 flow of 50 mL·min^{-1}. The material was reduced at 750 °C (550 °C for Ni−SiO_2) for 1.5 h under 5% H_2 in N_2 at a flow rate of 70 mL·min^{-1}. After reduction, the material was cooled to 550 °C at a rate of 10 °C·min^{-1} in N_2 at a flow of 50 mL·min^{-1}. The extent of carbon formation was studied at 550 °C using 10% CH_4 in N_2 at a flow of 30 mL·min^{-1} for 30 min.

2.4. SE-SMR Test. The SE-SMR reaction was studied in the laboratory-scale packed-bed reactor depicted in Figure S1 of the Supporting Information. The reactor (i.d. 9.7 mm, total length 411 mm) was made of stainless steel and contained a perforated plate to support the bed. The reactor was placed in a tubular furnace, the temperature of the bed being controlled via an N-type thermocouple. The gas was fed from the top of the reactor. A layer of Al_2O_3 on top of the bed of active material was used to preheat the gas. The flow rate of the feed gases—(i) 5% H_2 in N_2, (ii) 10% CH_4 in N_2, and (iii) N_2—were recorded using calibrated mass flow meters (AWM5101VN, Honeywell). Steam was generated by feeding liquid water via a syringe pump into an evaporator maintained at 220 °C. Switching between different atmospheres was achieved via computer-controlled solenoid valves. The outlet gas was dried first by condensation via an ice bath and subsequently via an anhydrous $CaCl_2$ trap. The gas composition of the effluent gas was analyzed continuously using (i) a nondispersive infrared analyzer measuring CO, CO_2, and CH_4 (ABB Uras26) and

dx.doi.org/10.1021/cs300247g | ACS Catal. 2012, 2, 1635−1646

(ii) a thermal conductivity analyzer measuring H_2 (ABB Caldos27). The carbon balance was closed within ±5%.

The following materials were studied for the SE-SMR reaction: (i) 5.18 g Ni−SO_2 + 1.26 g calcined limestone, (ii) 5.7 g Ni-ex-Htlc +1.26 g calcined limestone, and (iii) 6 g Ca−Ni-ex-Htlc. The mass of the materials was chosen such that in each experiment, 22.5 mmol CaO and 46.0 mmol Ni were used. For the cases that a Ni catalyst was used together with limestone, the CO_2 sorbent and the catalyst were premixed prior to being placed in the packed bed reactor. First, the bed was reduced in a flow of 1.0 L·min^{-1} H_2 at 750 °C for 2 h (Ni-ex-Htlc and Ca−Ni-ex-Htlc) or at 550 °C for 20 min (Ni−SiO_2). As shown later, a reduction of Ni−SiO_2 at 750 °C would destroy its activity. The catalyst was not reduced between subsequent SE-SMR cycles.

The complete reduction of nickel under the reduction conditions applied was confirmed by the continuously monitored H_2 concentration. Subsequently, the SE-SMR reaction was performed at 550 °C using a flow of 0.56 L·min^{-1} of 10% CH_4 in N_2. The steam to methane ratio was 4. The operating conditions chosen are in agreement with previous studies investigating the sorbent-enhanced steam reforming reaction using CaO as the CO_2 sorbent.[5,9,42] After 12 min, the flow of CH_4 and steam was stopped, and the bed was switched back to pure N_2 with a flow rate of 0.8 L·min^{-1}. To calcine the carbonated CO_2 sorbent, the temperature of the bed was increased to 750 °C. After completion of the calcination reaction (~15 min), the temperature of the bed was reduced to 550 °C, and a new cycle was started. In total, 10 (Ni-ex-Htlc and Ca−Ni-ex-Htlc) or 5 (Ni−SiO_2) cycles were performed.

3. RESULTS AND DISCUSSION

3.1. Characterization of the Fresh Catalyst. The crystalline phases of the fresh (as), calcined (calc) and reduced (red) materials were determined using XRD. The diffractograms of the fresh as-Ni-ex-Htlc and as-Ca−Ni-ex-Htlc, shown in Figure 1, indicate the presence of hydrotalcite ($Mg_6Al_2CO_3(OH)_{16}\cdot 4H_2O$) and takovite ($Ni_6Al_2(OH)_{16}(CO_3,OH)\cdot 4H_2O$). The peaks located at 2θ ≅ 11, 23, and 35° correspond to the (003), (006), and (009) crystal planes, respectively.[43] Additional peaks located at 2θ ≅ 39, 47, 61, and 63° correspond to the (015), (018), (110), and (113) crystal planes.[43,44] In as-Ca−Ni-ex-Htlc, Ca^{2+} is present as calcite, the thermodynamically stable polymorph of $CaCO_3$. On the other hand, in the diffractrogram of (unreduced) as-Ni−SiO_2, only NiO diffraction patterns can be observed because of the amorphous nature of silica.

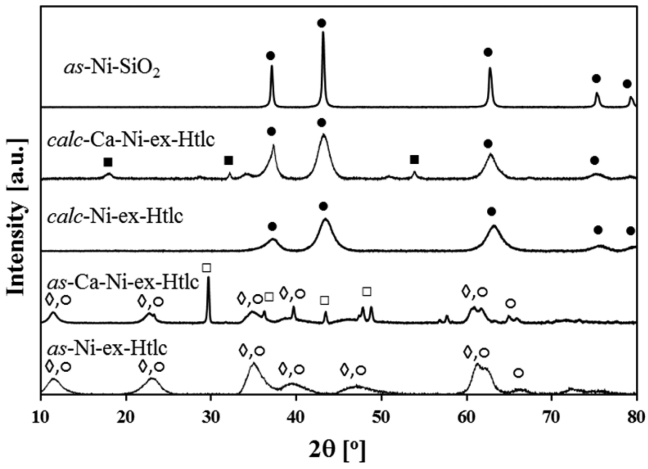

Figure 1. X-ray diffraction patterns of freshly prepared and calcined nickel-based catalysts. The following compounds were identified: (◊) hydrotalcite, $Mg_6Al_2CO_3(OH)_{16}\cdot 4H_2O$; (○) takovite, $Ni_6Al_2(OH)_{16}(CO_3,OH)\cdot 4H_2O$; (□) calcite, $CaCO_3$; (●) bunsenite; NiO; and (■) portlandite, $Ca(OH)_2$.

After calcination in N_2 at 800 °C, the hydrotalcites are transformed into oxides of Mg, Al, and Ni. The formation of mixed oxides of Ca^{2+} and Al^{3+}, such as mayenite ($Ca_{12}Al_{14}O_{33}$), was not detected in the diffractogram of calc−Ca−Ni-ex-Htlc. For calc-Ni− and calc-Ca−Ni-ex-Htlc, the peaks located at 37, 43, 63, 75, and 79° were assigned to NiO; however, since MgO (lattice parameter a = 4.22 Å, NaCl structure[45]) and NiO (lattice parameter a = 4.18 Å, NaCl structure[46]) are isomorphous, it is not possible to exclude the formation of a mixed oxide (i.e., $Mg_xNi_{1-x}O$), which has been proposed in previous studies.[47] However, the formation of the spinel $MgAl_2O_4$ could not be detected in calc-Ni− or calc−Ca−Ni-ex-Htlc. As expected, the diffractograms of the reduced catalysts (Figure S2, Supporting Information) show the presence of Ni with a very small amount of NiO due to the formation of a passivation layer. Since MgO and NiO are isomorphous, the peaks of NiO, $NiAl_2O_4$, and $MgNiO_2$ overlap with the peak of MgO also for the reduced catalysts. Using the Scherrer equation, the crystallite size of CaO in red−Ca−Ni-ex-Htlc was determined as 25 nm. Owing to the small size of the CaO peaks in the diffractogram of red−Ca−Ni-ex-Htlc, some CaO may be present as an amorphous phase.

The BET surface area, pore volume, and pore diameter of the CO_2 sorbents and the calcined and reduced catalysts are summarized in Table 1. Calcined Ni-ex-Htlc and Ca−Ni-ex-Htlc possessed a high surface area of 210 and 120 m^2·g^{-1}, respectively, but upon reduction with H_2 at 750 °C, the surface area decreased to 126 and 54 m^2·g^{-1}, respectively. Owing to the low Tammann temperature of Ni of 691 °C[48] when compared with the Tammann temperatures of NiO (856 °C[49]), CaO (1376 °C[27]), and $MgAl_2O_4$ (1530 °C[50]), we believe that the reduction in surface area of the reduced catalysts is due to the sintering of Ni particles. Of the reduced catalysts, the highest surface area of 160 m^2·g^{-1} was determined for reduced Ni−SiO_2.

Comparing the surface areas of reduced Ca−Ni-ex-Htlc and Ni-ex-Htlc leads to the conclusion that the addition of Ca^{2+} results in a substantial reduction of surface area. Indeed, the reduction of the surface area of common support materials, such as Al_2O_3, via the addition of Ca^{2+} has been reported previously[23,24] and is a challenge in the synthesis of high-surface-area, Ca-based CO_2 sorbents. On the other hand, the addition of Ca^{2+} into the nickel hydrotalcite structure did not influence the pore volume appreciably. A high pore volume of 0.33, 0.26, and 0.23 cm^3·g^{-1} was measured for reduced Ni−SiO_2, Ni-ex-Htlc, and Ca−Ni-ex-Htlc, respectively. As discussed further below, a high and thermally stable pore volume is crucial for the development of Ca-based CO_2 sorbent, which possess a high and stable CO_2 uptake. Interestingly, the average pore diameter was fairly similar for all three unreacted, reduced catalysts: ranging between 7.1 and 12.1 nm. In contrast, calcined, naturally occurring limestone is characterized by a low surface area and pore volume and a comparatively small average pore diameter of 14 m^2·g^{-1}, 0.12 cm^3·g^{-1}, and 3.2 nm,

dx.doi.org/10.1021/cs300247g | ACS Catal. 2012, 2, 1635−1646

Table 1. Characterization of the Fresh Catalysts Reduced at 750 °C (550 °C for Ni−SiO_2) and Limestone

	Ni−SiO_2	Ni-ex-Htlc[a]	Ca−Ni-ex-Htlc[b]	limestone
Ni loading (wt %)	52	47	45	
BET surface area ($m^2 \cdot g^{-1}$)	160	126	54	14
BJH pore volume ($cm^3 \cdot g^{-1}$)	0.33	0.26	0.23	0.12
pore diameter (nm)	8.3	7.1	12.1	3.2
surface Ni (mmol/g)	0.23 ± 0.008	0.838 ± 0.018	0.634 ± 0.02	
Ni particle size (nm)	70.4 ± 2.5	14.7 ± 0.3	20.4 ± 0.5	
dispersion	2.38 ± 0.08	9.11 ± 0.2	6.89 ± 0.15	
Ni particle size (nm) (TEM)		26.0	28.9	

[a]The BET surface area, pore volume, and pore diameter in its calcined unreduced form was 210 $m^2 \cdot g^{-1}$, 0.40 $cm^3 \cdot g^{-1}$, and 6.0 nm, respectively. [b]The BET surface area, pore volume, and pore diameter in its calcined unreduced form was 120 $m^2 \cdot g^{-1}$, 0.41 $cm^3 \cdot g^{-1}$, and 6.9 nm, respectively.

respectively, indicating a very different morphology when compared with the synthetic Ca-based material.

The particle size, dispersion, and amount of active surface Ni calculated from H_2 chemisorption measurements are summarized in Table 1. In the reduced catalysts, the dispersion and active surface area of Ni increased according to Ni−SiO_2 < Ca−Ni-ex-Htlc < Ni-ex-Htlc, and the estimated size of the Ni particles increased consequently in the following order: Ni-ex-Htlc < Ca−Ni-ex-Htlc ≪ Ni−SiO_2. The Ni particles in Ni−SiO_2 are ∼3.5 and 4.8 times larger than for Ca−Ni-ex-Htlc and Ni-ex-Htlc, respectively. It seems that the addition of Ca^{2+} to Ni-ex-Htlc somewhat reduces the dispersion of Ni, an effect that is probably connected to the lower surface area of Ca−Ni-ex-Htlc. A transmission electron micrograph of the reduced Ca−Ni-ex-Htlc is given in Figure 2a, showing clearly well

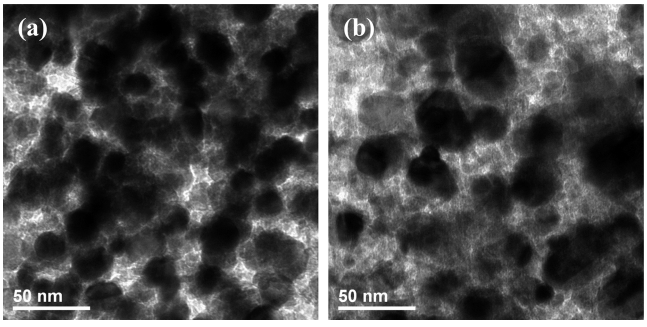

Figure 2. TEM images of (a) freshly reduced Ca−Ni-ex-Htlc and (b) reacted Ca−Ni-ex-Htlc.

dispersed Ni particles in the (Ca:Mg:Al)O_x matrix as typically observed.[47,51] The size of the Ni particles determined from TEM measurements is in fair agreement with H_2 chemisorption measurements reported in Table 1. Transmission electron micrographs of Ni−SiO_2 indicated very large and heterogeneous particles with sizes varying from 50 to 250 nm, confirming the low average nickel dispersion obtained by H_2 chemisorption.

Figure 3 shows the TPR profiles of (i) Ni−SiO_2, (ii) Ni-ex-Htlc, and (iii) Ca−Ni-ex-Htlc using H_2 as the reducing gas. For Ni−SiO_2, reduction starts at ∼300 °C, with a peak located at ∼410 °C, followed by a second, broader peak located at ∼540 °C. On the other hand, the reduction of hydrotalcite-based catalysts starts at substantially higher temperatures. For Ni− and Ca−Ni-ex-Htlc, reduction started at 580 and 600 °C, respectively, with single peaks located at 800 and 820 °C. For Ni catalysts supported on SiO_2, the occurrence of two peaks, located at ∼400 and ∼500 °C, has been observed previously

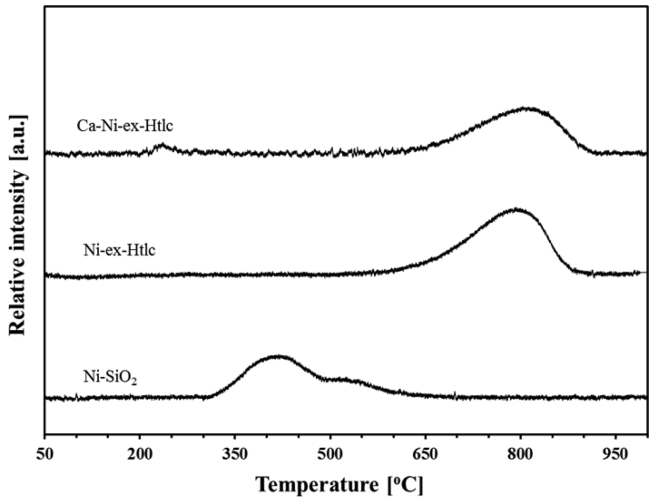

Figure 3. TPR measurements of the three catalysts studied. The catalysts were reduced in 5% H_2 in N_2 at a flow of 70 $mL \cdot min^{-1}$, and the temperature increase was 10 $°C \cdot min^{-1}$.

and was attributed to two different levels of catalyst−support interactions.[52] The peak located at ∼400 °C is due to the reduction of large crystals of bulk NiO. Such NiO has only weak interactions with the SiO_2 support, since the reduction of unsupported NiO occurs at the same temperature.[52] The peak at 500 °C has been attributed to either the reduction of small NiO crystallites with stronger catalyst−support interaction or the reduction of amorphous nickel silicates or nickel hydrosilicates.[52] The presence of only one, high-temperature reduction peak for Ni-hydrotalcite structures has been attributed to the reduction of well-dispersed Ni^{2+} embedded in the mixed oxide $Mg_xNi_{1-x}O$.[44,47] With regard to the higher reduction temperature of Ca−Ni-ex-Htlc, we speculate that the presence of Ca^{2+} influences the reducibility of Ni^{2+} via the formation of $Ca_yMg_xNi_{1-x-y}O$. Indeed, a shift in the reduction temperature of Ni-ex-Htlc-based catalysts to higher temperatures upon the addition of additional compounds has been reported previously.[53]

3.2. Materials Carbon Dioxide Absorption Properties.

The cyclic conversion of CaO into $CaCO_3$ of calcined and reduced Ca−Ni-ex-Htlc and limestone was determined in a TGA. For limestone, 84% of the available CaO reacts with CO_2 to form $CaCO_3$ in the first cycle (Figure 4); however, with cycle number, the cyclic conversion of CaO dramatically drops, reaching only 42% in the 10th cycle. Figure 4 shows that the calcined and reduced Ca−Ni-ex-Htlc possessed a high initial CaO conversion of 87 and 81%, corresponding to 0.14 and 0.13 g CO_2/g sorbent, respectively. The somewhat lower CaO

dx.doi.org/10.1021/cs300247g | ACS Catal. 2012, 2, 1635−1646

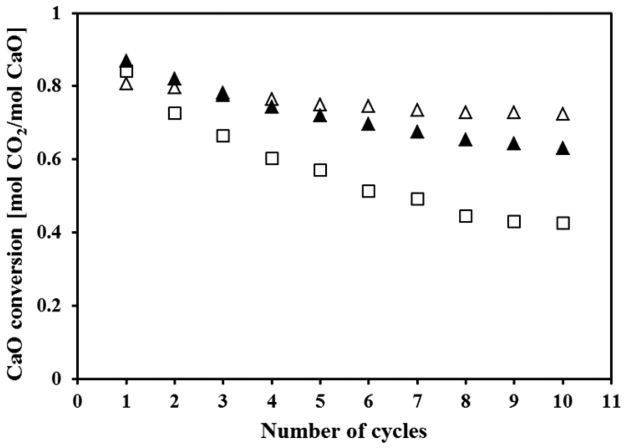

Figure 4. Cyclic conversion of CaO to $CaCO_3$ for (□) limestone, (▲) calcined Ca−Ni-ex-Htlc, and (Δ) reduced Ca−Ni-ex-Htlc. The carbonation and calcination reactions were performed isothermally at 750 °C. The carbonation reaction was performed for 20 min in an atmosphere containing 40 vol % CO_2 and 60 vol % N_2.

conversion in reduced Ca−Ni-ex-Htlc may be due the lower pore volume in reduced Ca−Ni-ex-Htlc, as shown in Table 1. However, reduced Ca−Ni-ex-Htlc showed a high cyclic stability of CaO conversion when compared with calcined Ca−Ni-ex-Htlc, reaching 72% after 10 cycles of carbonation and calcination.

The formation of $CaCO_3$ in Ca−Ni-ex-Htlc after the carbonation step was confirmed by XRD (Figure S3, Supporting Information). Performing the same experiment using Ni-ex-Htlc showed a negligible CO_2 uptake of Ni-ex-Htlc at the operating temperatures studied here. Generally, the decay in CaO conversion of Ca−Ni-ex-Htlc is less pronounced than for limestone. The rapid decay of the cyclic CO_2 capture capacity of limestone is well documented[17,24,54,55] and has been attributed to sintering due to the low Tammann temperature of $CaCO_3$ of 533 °C,[15] accompanied by severe, detrimental alterations in the pore structure.[16,17]

3.3. Sorbent-Enhanced Steam Methane Reforming of Ni−CO_2 Sorbent Systems. Subsequently, the different catalysts and CO_2 sorbents were investigated with regard to their cyclic activity for the SE-SMR reaction. The following materials were used: (i) Ni−SiO_2/calcined limestone (weight ratio of 4.1:1), (ii) Ni-ex-Htlc/calcined limestone (weight ratio of 4.5:1), and (iii) Ca−Ni-ex-Htlc. The mass of the materials was chosen such that in each experiment, the same amounts of CaO and Ni were used: 22.5 and 46.0 mmol, respectively. The SE-SMR reaction was performed at 550 °C with a steam-to-methane ratio of 4. Regeneration of the CO_2 sorbent was performed at 750 °C in a N_2 atmosphere.

Figure 5 shows the mole fractions of CH_4, CO, H_2, and CO_2 (dry basis) in the effluent gas of the packed bed reactor in the first and 10th cycles (5th for Ni−SiO_2) for the three material combinations investigated. Using a Gibbs free-energy minimization routine, thermodynamic equilibrium calculations of the SE-SMR reaction at 550 °C predict equilibrium mole fractions of H_2 and CH_4 of 0.28 and 0.008, respectively. These values are in close agreement with the values plotted in Figure 5, indicating that under the conditions studied here, thermodynamic equilibrium is achieved.

Ni−SiO_2 is clearly not a suitable catalyst for the SE-SMR reaction because of its dramatic loss in activity after the first

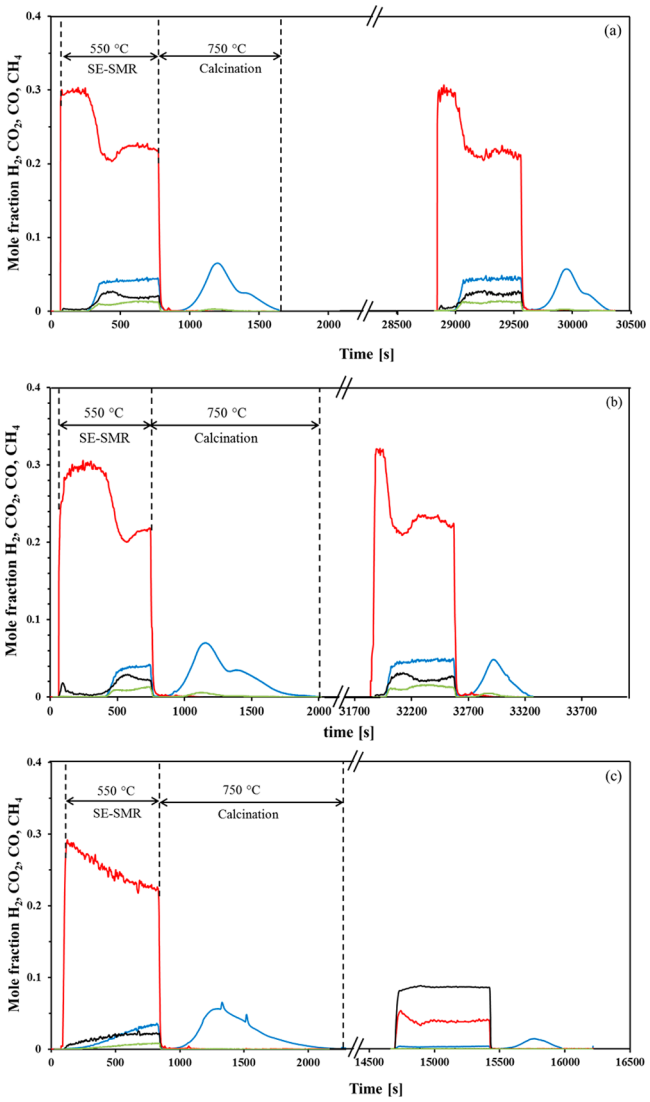

Figure 5. Composition of the effluent gas for the first and 10th (5th for Ni−SiO_2) cycles of the SE-SMR reaction: (a) Ca−Ni-ex-Htlc, (b) Ni-ex-Htlc, and (c) Ni−SiO_2. The experiments were performed at atmospheric pressure using a steam-to-methane ratio of 4. The flow rates of methane and nitrogen were 56 and 504 mL/min, respectively. In each experiment, the weights of Ni and CaO were kept constant at 2.7 and 1.26 g with the ratio of [gNi/gCaO] being 2.

regeneration step of $CaCO_3$, performed at 750 °C in N_2. It is known that Ni supported on SiO_2 has a lower stability when compared with Ni supported on Al_2O_3 for temperatures exceeding 650 °C. The loss of activity at elevated temperatures for such a catalytic system has been attributed to the growth of Ni particles and potentially higher rates of carbon formation.[56−58] The H_2 chemisorption measurements of reacted Ni−SiO_2 (Table 2) indicates a 3.1-fold decrease in the Ni dispersion after only five cycles, corresponding to an increase in the average size of the Ni particles from ∼70 to ∼265 nm. Considering the high activity of Ni−SiO_2 at the end of the first cycle, it can be concluded that the recalcination step at an elevated temperature of 750 °C is responsible for the deactivation of Ni−SiO_2.

The loss of active sites due to nickel sintering is probably not the only cause of activity loss. The coverage of surface nickel by carbon or silicates, typically observed in the presence of steam

dx.doi.org/10.1021/cs300247g | ACS Catal. 2012, 2, 1635−1646

Table 2. Characterisation of the reacted catalysts and limestone. The measurements were performed after 5 cycles for Ni−SiO_2 and 10 cycles Ni-ex-Htlc, Ca−Ni-ex-Htlc and limestone

	Ni−SiO_2	Ni-ex-Htlc	Ca−Ni-ex-Htlc	limestone
BET surface area ($m^2 \cdot g^{-1}$)	160	72	54	9
BJH pore volume ($cm^3 \cdot g^{-1}$)	0.34	0.23	0.27	0.07
pore diameter (nm)	8.1	9.2	12.1	30
surface Ni (mmol/g)	0.074 ± 0.002	0.408 ± 0.009	0.370 ± 0.011	
Ni particle size (nm)	264.9 ± 8.6	34.0 ± 0.8	38.2 ± 0.9	
dispersion (%)	0.77 ± 0.024	4.44 ± 0.10	4.02 ± 0.09	
Ni particle size (nm) TEM		31.1	31.7	

and high temperatures, probably also contributes to the dramatic deactivation of Ni−SiO_2.[59,60] On the other hand, Ca−Ni-ex-Htlc consists of Ni and CaO nanoparticles ∼20 and 25 nm in size, respectively, supported on a high Tammann temperature, inert $(Mg:Al)O_x$ matrix. Owing to the high pore volume of Ca−Ni-ex-Htlc of 0.23 $cm^3 \cdot g^{-1}$, CaO is highly accessible. Considering that at a product layer thickness of 50 nm, diffusion limitation becomes significant, CaO nanoparticles of <100 nm in size should be carbonated in the fast reaction regime. This is confirmed by the TGA plot given in Figure 8c. In addition, the incorporation of Ni particles in the $(Mg:Al)O_x$ matrix effectively stabilized Ni particles and reduced particle agglomeration, resulting in catalysts of stable activity.

For practical applications, the shape of the breakthrough curve of the SE-SMR reaction is an important aspect, since impurities of CO_2 or CO will necessitate further gas cleanup steps. Here, the breakthrough of CO, CO_2, and CH_4 refers to the transition from SE-SMR to the conventional methane steam reforming reaction once the CO_2 sorbent has been depleted. Figure 6a and b plot the breakthrough behavior for the first, fifth, and 10th cycles of Ca−Ni-ex-Htlc and Ni-ex-Htlc, respectively. From Figure 6, the following features can be observed:

- In the prebreakthrough stage (e.g. t = 0−250 s for the first cycle of Ca−Ni-ex-Htlc), the mole fractions of CO_2, CO, and CH_4 are very low, whereas the yield of hydrogen is very high, implying that CO_2 is quickly abstracted by the formation of $CaCO_3$, thus shifting the conversion of CH_4 and CO via, respectively, the steam methane reforming and water-gas-shift reaction to the product side. Considering that the CO_2 slip is negligible, it can be concluded that the carbonation reaction is fast, reaching thermodynamic equilibrium. As envisaged, high-purity hydrogen is produced in this reaction stage without further gas cleanup.
- During the breakthrough stage, defined as the time period in which the mole fraction of H_2 reduces from ∼0.29 to 0.21 (e.g., t = 250−400 s for the first cycle of Ca−Ni-ex-Htlc), the fraction of CO_2 in the effluent stream gradually increases. In parallel, a decrease in methane conversion and hydrogen yield together with an increase in the mole fraction of CO are observed. In the breakthrough stage, the reaction of CO_2 with CaO is controlled by diffusion rather than equilibrium thermodynamics. At the end of the breakthrough stage, the mole fraction of CO_2 is close to its equilibrium value for the combined steam methane reforming (1) and water-gas-shift (2) reactions of ∼0.047.

Also for Ni-ex-Htlc, a fairly sharp increase in the mole fraction of carbon dioxide in the breakthrough stage was observed. For Ca−Ni-ex-Htlc, the time at which the breakthrough occurs decreased from ∼250 s to ∼160 s between the first and fifth cycles. However, between the fifth and 10th cycles, only a small decrease from 160 to 150 s was observed, indicating comparatively stable CO_2 uptakes. This observation is in agreement with the cyclic CO_2 uptake characteristics of Ca−Ni-ex-Htlc shown in Figure 4. Overall, the sharp breakthrough characteristics prevail throughout all cycles. On the other hand, for Ni-ex-Htlc + limestone (Figure 6b), the time at which the breakthrough occurred continuously decreased from 310 to 170 s and 75 s in the first, fifth, and 10th cycles, respectively. Indeed, for Ni-ex-Htlc, the onset of breakthrough continuously shifts toward earlier times, with an

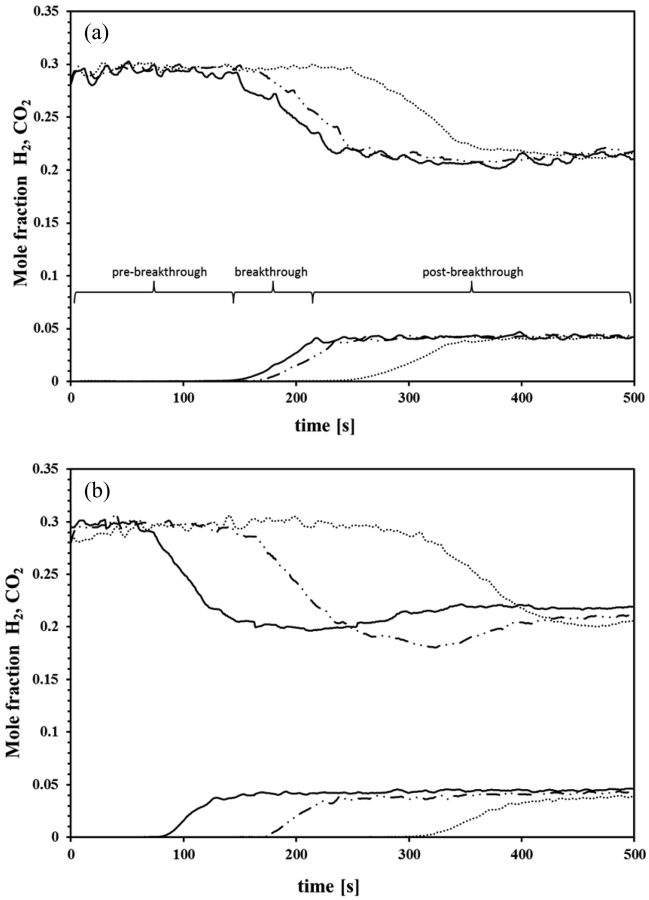

Figure 6. Breakthrough curves using (a) Ca−Ni-ex-Htlc and (b) Ni-ex-Htlc + limestone: (····) 1st cycle, (– · ·) 5th cycle, and (—) 10th cycle. The SE-SMR reaction was performed at 550 °C using a flow of 0.56 $L \cdot min^{-1}$ of 10 vol % CH_4 in N_2. The steam-to-methane ratio was 4, and the calcination reaction was performed at 750 °C. The prebreakthrough, breakthrough, and postbreakthrough stages are marked for the 10th cycle in Figure 7a.

dx.doi.org/10.1021/cs300247g | ACS Catal. 2012, 2, 1635−1646

almost constant rate. After the 10th cycle, the prebreakthrough duration of Ca−Ni-ex-Htlc is 200% longer than for Ni-ex-Htlc. The duration of the prebreakthrough period will be predominantly governed by the extent of the first stage of the carbonation reaction, that is, the filling of volume available in small pores (d_{pore} < 100 nm) by freshly formed $CaCO_3$. On the other hand, the duration of the breakthrough period depends on the extent of the second, slower stage of the carbonation reaction, the kinetics of which are governed by the slow diffusion of CO_2 through a thick product layer of $CaCO_3$.

Using the mole fraction of CO_2 in the calcination step and the mole fraction of H_2 during the prebreakthrough stage, the quantities of hydrogen produced and carbon dioxide captured during SE-SMR operation were calculated, and their evolution with the number of cycles is presented in Figure 7. It can be

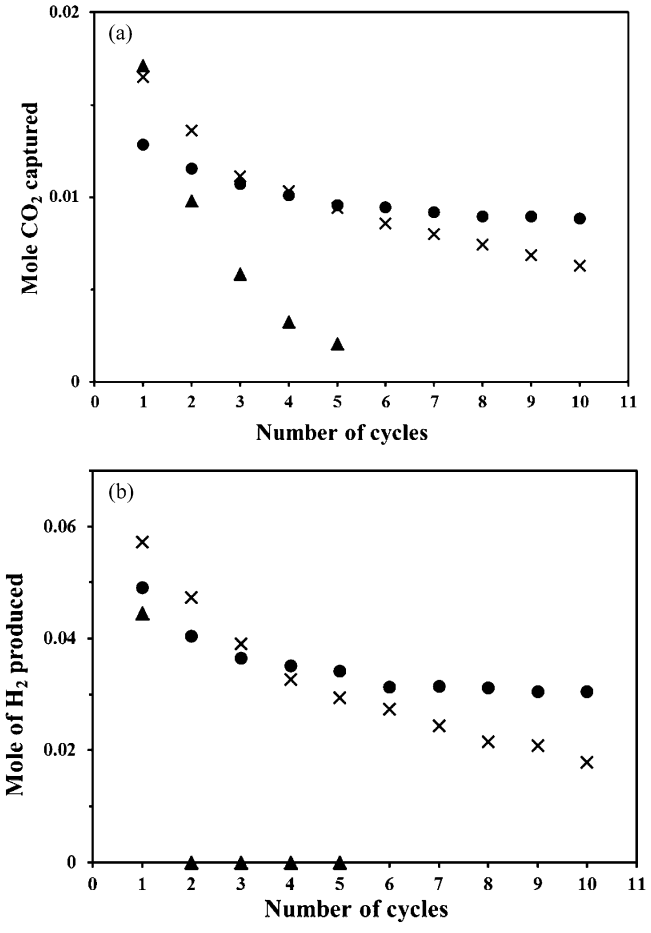

Figure 7. Cyclic (a) CO_2 uptake and (b) H_2 production: (▲) Ni−SiO_2, (×) Ni-ex-Htlc, and (●) Ca−Ni-ex-Htlc.

seen that Ni−SiO_2 performed well only in the first cycle and significantly lost its activity in subsequent cycles. Both Ni-ex-Htlc and Ca−Ni-ex-Htlc performed well, with Ca−Ni-ex-Htlc exceeding the performance of Ni-ex-Htlc on the basis of the absolute quantity of CO_2 captured and, in particular, H_2 produced starting from the fifth cycle. In addition, Ca−Ni-ex-Htlc also possessed good cyclic stability when compared with Ni-ex-Htlc, reaching a rather stable prebreakthrough production of hydrogen after three cycles, whereas the Ca-free hydrotalcite-based catalyst further deactivates. The reason for the difference in the two catalysts in the quantity of hydrogen produced is directly connected to the breakthrough characteristics: the Ni-ex-Htlc absorbed CO_2 without producing high-purity H_2 for much longer than Ca−Ni-ex-Htlc.

It is worth mentioning that Ca−Ni-ex-Htlc was not optimized with regard to maximal CO_2 capture, but the focus of this study was to demonstrate the possibility to functionalize the Ni catalyst with a Ca-based CO_2 sorbent to allow excellent heat and mass transfer within a single grain The experimental results obtained here further demonstrated (i) a high cyclic CaO conversion and (ii) fast carbonation kinetics in Ca−Ni-ex-Htlc.

These favorable CO_2 capture characteristics of Ca−Ni-ex-Htlc can be explained by the existence of two regimes of the carbonation reaction,[61] which are sketched schematically in Figure 8. In the first, fast reaction stage, pore volume available in pores of diameter <100 nm is filled. The importance of the available pore volume for the carbonation reaction becomes clear if the molar volume of the product, $CaCO_3$ (V_M = 36.9 $cm^3\ mol^{-1}$) is compared with the molar volume of the reactant CaO (V_M = 16.7 $cm^3\ mol^{-1}$). The first reaction stage is characterized by a rapid, almost linear, weight increase in the CO_2 sorbent with time. Once the pore volume is filled, the second, substantially slower, reaction stage takes over. In the second reaction stage, a product layer of $CaCO_3$ is deposited on the outside of unreacted grains of CaO.[61−64] Thus, slow diffusion processes through the dense layer of $CaCO_3$ control the further reaction of CaO. Alvarez and Abanades[62] estimated that at a critical product layer thickness of ∼50 nm, the transition from the fast to the slow reaction state occurs. The transition between the two carbonation regimes is marked in the TGA graph, plotting the degree of carbonation as a function of time for limestone (Figure 8c).

Fresh limestone consists of grains ∼2−20 nm in size, with intragrain pores forming upon its calcination.[6] Since naturally occurring limestone consists of 100% $CaCO_3$, sintering and large structural changes during carbonation−calcination cycles result in a substantial loss of intragrain pore volume and, thus, a reduced CO_2 uptake in the first, fast reaction stage at subsequent cycles.[17] Indeed, a direct correlation between the pore volume available in pores <100 nm and the CO_2 uptake has been proposed.[65] These dramatic changes in the structure of limestone are documented in Table 2. After 10 cycles, the pore volume of limestone was reduced from an initial value of 0.12 $cm{\cdot}g^{-1}$ to only 0.07 $cm^3{\cdot}g^{-1}$. In addition, the average pore diameter increased by almost a magnitude from 3.2 to 30.0 nm.

On the other hand, Ca−Ni-ex-Htlc is composed of Ni and CaO nanoparticles ∼20 and 25 nm in size, respectively, supported on a high Tammann temperature,[53] inert $(Mg:Al)O_x$ matrix. In addition, owing to the high pore volume of Ca−Ni-ex-Htlc of 0.23 $cm^3{\cdot}g^{-1}$, CaO is highly accessible. Considering that at a product layer thickness of 50 nm, diffusion limitation becomes significant, CaO nanoparticles of <100 nm in size should be carbonated in the fast reaction regime. This is confirmed by the TGA plot given in Figure 8c. Importantly, the structure of Ca−Ni-ex-Htlc was confirmed by N_2 adsorption measurements (Tables 1 and 2) to be stable over 10 SE-SMR cycles, that is, the pore volume, surface area, and pore diameter were stable with cycle number. Thus, it can be expected that also in the 10th SE-SMR cycle, the dominating amount of CO_2 is captured in the fast carbonation regime, as demonstrated in Figures 4 and 5. Supporting CaO on a finely dispersed, high-melting point material, such as Al_2O_3, has been shown recently to stabilize CaO grains and reduce sintering.[22−24,65−67] The fact that Ca−Ni-ex-Htlc captured almost the entire amount of the

dx.doi.org/10.1021/cs300247g | ACS Catal. 2012, 2, 1635−1646

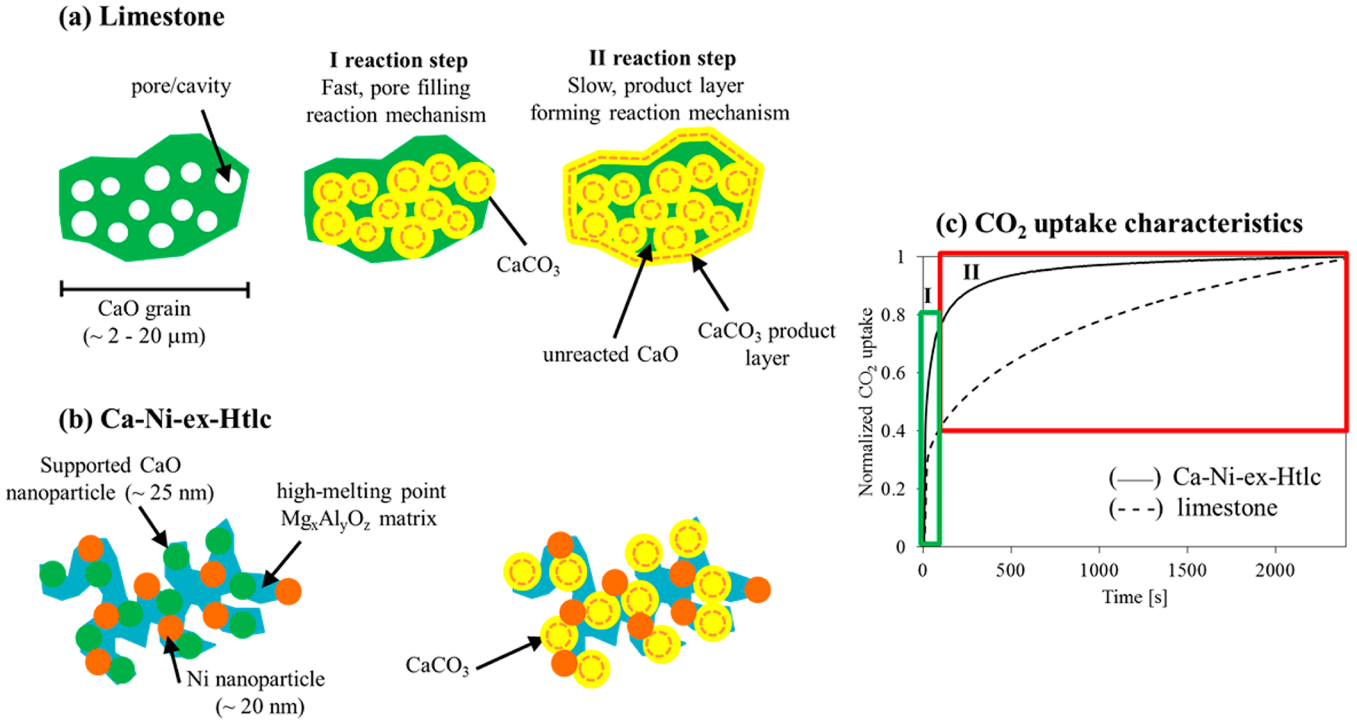

Figure 8. Schematic diagram of the reaction regimes occurring during the carbonation of CaO-based CO_2 sorbents: (a) naturally occurring limestone and (b) Ca−Ni-ex-Htlc. The transition between the first and second reaction stages is marked in a typical carbonation graph plotting the normalized CO_2 uptake as a function of time (c).

CO_2 over 10 cycles in the fast, practically relevant reaction stage, resulted in a very sharp, and from the fifth cycle number stable, breakthrough curve. On the other hand, the breakthrough of CO_2 in Ni-ex-Htlc + limestone continuously shifted with cycle number to shorter times, since limestone rapidly loses its capability to capture a large amount of CO_2 that is captured in the first and fast reaction stage.

The CO_2 uptake of Ca−Ni-ex-Htlc under SE-SMR conditions is lower compared with the CO_2 uptake determined from TGA experiments using a mixture of CO_2 and N_2. Sultana and Chen[42] also reported that simple TGA-based CO_2 capture experiments cannot be used to predict the CO_2 uptake under SE-SMR conditions. Possible reasons for the lower CO_2 uptake under SE-SMR conditions are (i) the lower reaction temperature, (ii) shorter duration time of the carbonation reaction, (iii) a lower CO_2 concentration,[17,68] and (iv) the presence of steam.

Bifunctional materials for the SE-SMR were studied by Satrio et al.[13] and Martavaltzi and Lemonidou.[14] However, both studies reported only one cycle of the SE-SMR reaction at a given temperature. Satorio et al.[13] reported a CO_2 uptake of 0.09 g CO_2/g sorbent, whereas Martavaltzi and Lemonidou[14] observed a 60% carbonation conversion of CaO in their material. The material developed here compares well with the previously reported sorbents, that is, possessing a CO_2 uptake of 0.09 g CO_2/g sorbent, corresponding to 57% CaO conversion in the first cycle. However, we also demonstrate the good stability of our material over 10 SE-SMR cycles.

3.4. The Effect of Calcium on Carbon Formation. Nickel-based catalysts are well-known for suffering from coking, a phenomenon that is typically promoted by a low steam-to-methane ratio as used in this study. However, increasing the steam-to-methane ratio would substantially increase the operational costs of the SE-SMR process. Carbon deposition at 550 °C on previously reduced catalysts (H_2) was determined in a TGA as the weight increase of the catalyst as a function of time. Here, the increase in the measured sample weight results from the formation of carbon from methane decomposition catalyzed by the reduced metal according to

$$CH_4 \leftrightarrow 2H_2 + C_{(s)} \quad (5)$$

From Figure 9a, it can be seen that for the first 250 s, the quantity of carbon deposited did not differ substantially among the different catalysts. However, for times $t > 250$ s, the quantity of carbon deposited on Ni−SiO_2 via the decomposition of CH_4 is substantially lower when compared with Ni− and Ca−Ni-ex-Htlc. In fact, for Ni−SiO_2, the rate of carbon formation decreased with the amount of carbon deposited. This observation is in agreement with previous Ni K-edge XAS studies on Ni−SiO_2, which indicated that the decrease in the methane decomposition rate on Ni−SiO_2 was due to the formation of nickel carbide, Ni_3C.[69] On the other hand, with the exception of the short induction period, the amount of carbon deposited increased linearly for Ni-ex-Htlc and Ca−Ni-ex-Htlc, indicating a constant rate of carbon formation. Interestingly, the rate of carbon formation is slightly higher for Ca−Ni-ex-Htlc when compared with Ni-ex-Htlc, a difference that might originate from the different nickel particle sizes in the catalysts. Indeed, it has been reported previously that within the nickel particle size range studied here, the coking rate increased with the size of the Ni particles.[56,70] A blank test performed on nickel-free Ca-ex-Htlc showed no weight increase.

For a better comparison of the catalysts, the rate of carbon formation was related to the quantity of active sites, that is, the quantity of surface nickel ($mol_C \cdot mol_{surface\ Ni}^{-1}$), as shown in Figure 9b. Here, the highest rate of carbon formation was observed for Ni−SiO_2. The quantity of carbon deposited on

dx.doi.org/10.1021/cs300247g | ACS Catal. 2012, 2, 1635−1646

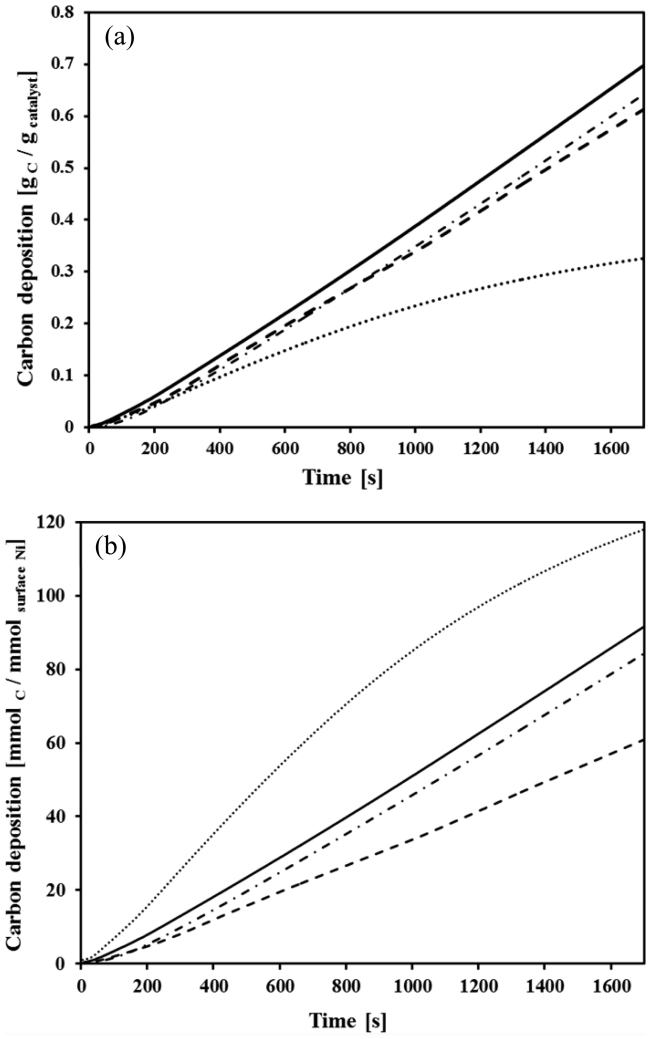

Figure 9. Carbon deposition via the decomposition at 550 °C as determined in a TGA. The catalysts were previously reduced in H_2 at 750 °C (550 °C for Ni−SiO_2). Carbon deposition is quantified as (a) $g_C \cdot g_{catalyst}^{-1}$ and (b) $mmol_C \cdot mmol_{surface\ Ni}^{-1}$. The initial mass of unreduced catalyst was ∼10 mg: (——) calcined Ca−Ni-ex-Htlc, (− · −) carbonated Ca−Ni-ex-Htlc, (····) Ni−SiO_2, and (− − −) Ni-ex-Htlc.

Ni−SiO_2 seemed to saturate at ∼140 $mol_C \cdot mol_{surface\ Ni}^{-1}$, a value indicating that C−C bonds (e.g., graphite) are formed along with nickel carbide. The two hydrotalcite-based catalysts showed a lower intrinsic rate of carbon formation rate than Ni−SiO_2 (Ni-ex-Htlc < Ca−Ni-ex-Htlc), with the quantity of C per surface nickel indicating again a large excess of carbon. To investigate whether the formation of $CaCO_3$ (during the SE-SMR CaO conversion into $CaCO_3$) has an influence on the formation of carbon, the same experiment was repeated for Ca−Ni-ex-Htlc in its carbonated form. The rate of carbon formation for carbonated Ca−Ni-ex-Htlc was reduced compared with calcined Ca−Ni-ex-Htlc (Figure 9a).

The effect of the addition of Ca, which is known to lead to the formation of basic (mixed) oxides, to Ni-based catalysts has been studied by several groups; however, conflicting results were reported, probably because of differences in the operating conditions used and the complexity of the catalytic systems studied.[71−75] However, it is generally agreed that carbonates formed on a support decrease the rate of carbon formation during reforming by providing O-based intermediates. Nevertheless, despite the formation of $CaCO_3$, the donation of O-based compounds is expected to be limited at 550 °C because of the stability of calcium carbonate. This would explain the limited reduction of the rate of carbon formation in the carbonated material. In addition, the distance between $CaCO_3$ particles and Ni particles has not yet been determined. A large separation of $CaCO_3$ and Ni could also explain the limited effect of support carbonation on carbon formation. Nevertheless, during the decarbonation (i.e. recalcination) at 750 °C, the release of CO_2 in close proximity of the nickel particles would favor the reverse Boudouard reaction, thus enabling coke scavenging. The latter argument is confirmed by the production of a small amount of CO during the calcination step (Figure 5), which can be attributed to the scavenging of C forming CO, the oxidation of nickel by CO_2, or both. Note that in this study, the influence of the presence of steam was neglected. Thus, further dedicated carbon formation studies are required to conclusively address the influence of Ca^{2+} on the formation of carbon under SE-SMR conditions.

4. CONCLUSIONS

We have developed a bifunctional catalyst for the sorbent-enhanced steam methane reforming (SE-SMR) reaction, synthesized via a coprecipitation technique. The material contained both the Ni catalyst (45 wt % Ni) and the Ca-based CO_2 sorbent (21 wt % CaO). At a temperature of 550 °C, S/C = 4, and a methane flow rate of 0.56 $L \cdot min^{-1}$, equilibrium conversion of methane was achieved, resulting in the production of high-purity hydrogen. Considering the high temperature used for the recalcination of $CaCO_3$ (750 °C), the dispersion of nickel on Ca−Ni-ex-Htlc decreased only slowly when compared to the Ni−SiO_2 catalyst or even Ni-ex-Htlc, demonstrating that the hydrotalcite-based matrix of Ca−Ni−Htlc effectively stabilized Ni particles toward sintering. In addition, Ca−Ni-ex-Htlc possessed a CO_2 absorption capacity that was significantly more stable during repeated carbonation/decarbonation cycles than for naturally occurring limestone. This was attributed to the highly stable and porous $(Al:Mg:Ca)O_x$ structure of the material on which the CaO particles are supported/embedded, stabilizing the CaO grains and reducing their sintering. Indeed, after 10 cycles of the SE-SMR reaction, the pore volume of Ca−Ni-ex-Htlc was 0.27 $cm^3 \cdot g^{-1}$, whereas the pore volume of limestone reduced to only 0.07 $cm^3 \cdot g^{-1}$ after 10 cycles, as a result of the loss of its fine structure. Furthermore, owing to the high dispersion and accessibility of CaO in Ca−Ni-ex-Htlc, CO_2 was captured almost entirely in the fast reaction stage, unlike for limestone, which lost its capability to capture a substantial amount of CO_2 in the first reaction stage with cycle number.

These favorable CO_2 capture characteristics lead to a very steep and, from the fifth cycle onward, stable breakthrough curve, that is, a sudden saturation of CaO with carbon dioxide leading a sharp switch from the SE-SMR regime to the conventional steam reforming reaction. A TG analysis of methane cracking at 550 °C on Ca−Ni-ex-Htlc indicated that its carbonation resulted in only a small reduction of the rate of carbon formation. This was attributed to a limited interaction between CaO and Ni or the high stability of $CaCO_3$ at the SE-SMR reaction temperature. However, the release of CO_2 during the decarbonation (i.e., the recalcination of $CaCO_3$) is believed to scavenge the coke formed via the reverse Boudouard

reaction, as indicated by the production of CO in the recalcination step.

A more detailed study of the effect of Ca on carbon formation has to be done, together with further improvements of the bifunctional catalyst. A particular focus will be on increasing the CaO content and the Ni dispersion in the hydrotalcite-based matrix, together with an enhanced contact of the sites of these two material sites.

■ ASSOCIATED CONTENT

Supporting Information

Additional information as noted in text. This material is available free of charge via the Internet at http://pubs.acs.org.

■ AUTHOR INFORMATION

Corresponding Author

*Phone: +41 44 632 3440. Fax: +41 44 632 14 83. E-mail: muelchri@ethz.ch.

Notes

The authors declare no competing financial interest.

■ ACKNOWLEDGMENTS

The authors are grateful to the Swiss National Science Foundation (SNF) for financial support (Project: 200021_135457/1). The authors also thank Mrs. Lydia Zehnder for help with the XRD measurements and the Electron Microscopy Center of ETH Zurich (EMEZ) for providing training and access to electron microscopes.

■ REFERENCES

(1) Cobden, P. D.; van Beurden, P.; Reijers, H. T. J.; Elzinga, G. D.; Kluiters, S. C. A.; Dijkstra, J. W.; Jansen, D.; van den Brink, R. W. *Int. J. Greenhouse Gas Control* **2007**, *1*, 170−179.
(2) Bohn, C. D.; Müller, C. R.; Cleeton, J. P. E.; Hayhurst, A. N.; Davidson, J. F.; Scott, S. A.; Dennis, J. S. *Ind. Eng. Chem. Res.* **2008**, *47*, 7623−7630.
(3) Mayorga, S. G.; Hufton, J. R.; Sircar, S.; Gaffney, T. R. *Sorption Enhanced Reaction Process for Production of Hydrogen. Phase 1 Final Report*; Air Products and Chemicals, Inc.: Allentown, PA, 1997.
(4) Balasubramanian, B.; Ortiz, A. L.; Kaytakoglu, S.; Harrison, D. P. *Chem. Eng. Sci.* **1999**, *54*, 3543−3552.
(5) Harrison, D. P. *Ind. Eng. Chem. Res.* **2008**, *47*, 6486−6501.
(6) Manovic, V.; Anthony, E. J. *Ind. Eng. Chem. Res.* **2010**, *49*, 9105−9110.
(7) Johnsen, K.; Grace, J. R.; Elnashaie, S. E. H.; Kolbiensen, L.; Eriksen, D. *Ind. Eng. Chem. Res.* **2006**, *45*, 4133−4144.
(8) Reijers, H. T. J.; Valster-Schiermeier, S. E. A.; Cobden, P. D.; van den Brink, R. W. *Ind. Eng. Chem. Res.* **2006**, *45*, 2522−2530.
(9) Ochoa-Fernandez, E.; Haugen, G.; Zhao, T.; Ronning, M.; Aartun, I.; Borresen, B.; Rytter, E.; Ronnekleiv, M.; Chen, D. *Green Chem.* **2007**, *9*, 645−662.
(10) Rostrup-Nielsen, T. *Catal. Today* **2005**, *106*, 293−296.
(11) Solieman, A. A. A.; Dijkstra, J. W.; Haije, W. G.; Cobden, P. D.; van den Brink, R. W. *Int. J. Greenhouse Gas Control* **2009**, *3*, 393−400.
(12) Choi, S.; Drese, J. H.; Jones, C. W. *ChemSusChem* **2009**, *2*, 796−854.
(13) Satrio, J. A.; Shanks, B. H.; Wheelock, T. D. *Ind. Eng. Chem. Res.* **2005**, *44*, 3901−3911.
(14) Martavaltzi, C. S.; Lemonidou, A. A. *Chem. Eng. Sci.* **2010**, *65*, 4134−4140.
(15) Judd, M. D.; Pope, M. I. *J. Appl. Chem.* **1970**, *20*, 384−388.
(16) Sun, P.; Grace, J. R.; Lim, C. J.; Anthony, E. J. *Chem. Eng. Sci.* **2008**, *63*, 57−70.
(17) Fennell, P. S.; Pacciani, R.; Dennis, J. S.; Davidson, J. F.; Hayhurst, A. N. *Energy Fuels* **2007**, *21*, 2072−2081.
(18) Manovic, V.; Anthony, E. J. *Energy Fuels* **2008**, *22*, 1851−1857.
(19) Manovic, V.; Anthony, E. J. *Environ. Sci. Technol.* **2008**, *42*, 4170−4174.
(20) Manovic, V.; Anthony, E. J. *Fuel* **2008**, *87*, 1564−1573.
(21) Fennell, P. S.; Davidson, J. F.; Dennis, J. S.; Hayhurst, A. N. *J. Energy Inst.* **2007**, *80*, 116−119.
(22) Filitz, R.; Kierzkowska, A. M.; Broda, M.; Müller, C. R. *Environ. Sci. Technol.* **2012**, *46*, 559−565.
(23) Kierzkowska, A. M.; Müller, C. R. *Energy Environ. Sci.* **2012**, *5*, 6061−6065.
(24) Broda, M.; Kierzkowska, A. M.; Müller, C. R. *ChemSusChem* **2012**, *5*, 411−418.
(25) Müller, C. R.; Pacciani, R.; Bohn, C. D.; Scott, S. A.; Dennis, J. S. *Ind. Eng. Chem. Res.* **2009**, *48*, 10284−10291.
(26) Chanburanasiri, N.; Ribeiro, A. M.; Rodrigues, A. E.; Arpornwichanop, A.; Laosiripojana, N.; Praserthdam, P.; Assabumrungrat, S. *Ind. Eng. Chem. Res.* **2011**, *50*, 13662−13671.
(27) Reddy, E. P.; Smirniotis, P. G. *J. Phys. Chem. B* **2004**, *108*, 7794−7800.
(28) Lu, H.; Reddy, E. P.; Smirniotis, P. G. *Ind. Eng. Chem. Res.* **2006**, *45*, 3944−3949.
(29) Gupta, H.; Fan, L. S. *Ind. Eng. Chem. Res.* **2002**, *41*, 4035−4042.
(30) Martavaltzi, C. S.; Lemonidou, A. A. *Microporous Mesoporous Mater.* **2008**, *110*, 119−127.
(31) Martavaltzi, C. S.; Pefkos, T. D.; Lemonidou, A. A. *Ind. Eng. Chem. Res.* **2011**, *50*, 539−545.
(32) Wang, M.; Lee, C. G.; Ryu, C. K. *Int. J. Hydrogen Energy* **2008**, *33*, 6368−6372.
(33) Qin, C.; Liu, W.; An, H.; Yin, J.; Feng, B. *Environ. Sci. Technol.* **2012**, *46*, 1932−1939.
(34) Manovic, V.; Anthony, E. J. *Environ. Sci. Technol.* **2009**, *43*, 7117−7122.
(35) Luo, C.; Zheng, Y.; Ding, N.; Wu, Q. L.; Zheng, C. G. *Chin. Chem. Lett.* **2011**, *22*, 615−618.
(36) Karami, D.; Mahinpey, N. *Ind. Eng. Chem. Res.* **2012**, *51*, 4567−4572.
(37) He, L.; Berntsen, H.; Ochoa-Fernandez, E.; Walmsley, J. C.; Blekkan, E. A.; Chen, D. *Top. Catal.* **2009**, *52*, 206−217.
(38) Brunauer, S.; Emmett, P. H.; Teller, E. *J. Am. Chem. Soc.* **1938**, *60*, 309−319.
(39) Barrett, E. P.; Joyner, L. G.; Halenda, P. P. *J. Am. Chem. Soc.* **1953**, *73*, 373−380.
(40) Kammler, Th.; Wehner, S.; Küppers, J. *Surf. Sci.* **1995**, *339*, 125−134.
(41) Bartholomew, C. H.; Pannell, R. B.; Butler, J. L. *J. Catal.* **1980**, *65*, 335−347.
(42) Sultana, K. S.; Chen, D. *Catal. Today* **2011**, *171*, 43−51.
(43) Cavani, F.; Trifiro, F.; Vaccari, A. *Catal. Today* **1991**, *11*, 173−301.
(44) Yu, J. J.; Jiang, Z.; Zhu, L.; Hao, Z. P.; Xu, Z. P. *J. Phys. Chem. B* **2006**, *110*, 4291−4300.
(45) Madelung, O.; Rössler, U.; Schulz, M. *Magnesium oxide (MgO) crystal structure, lattice parameters, thermal expansion*; The Landolt−Brnstein Database (http://www.springermaterials.com), vol. III/17B-22A-41B, SpringerMaterials.
(46) Bertel, L. C.; Morosin, B. *Phys. Rev. B* **1971**, *3*, 1039−1943.
(47) Ochoa-Fernandez, E.; Lacalle-Vila, C.; Christensen, K. O.; Walmsley, J. C.; Rønning, M.; Holmen, A.; Chen, D. *Top. Catal.* **2007**, *45*, 3−8.
(48) Sharma, A.; Saito, I.; Nakagawa, H.; Miura, K. *Fuel* **2007**, *86*, 915−920.
(49) Carreon, M. A.; Guliants, V. V. *Eur. J. Inorg. Chem.* **2005**, 27−43.
(50) Carniglia, S. C.; Barna, G. L. *Handbook of Industrial Refractories Technology: Principles, Types, Properties and Application*; William Andrew Publishing/Noyes: New York, 1992.
(51) Ochoa-Fernández, E.; Rusten, H. K.; Jakobsen, H. A.; Rønning, M.; Holmen, A.; Chen, D. *Catal. Today* **2005**, *106*, 41−46.
(52) Mile, B.; Stirling, D.; Zammitt, M.; Lovell, A.; Webb, M. *J. Catal.* **1988**, *114*, 217−219.

(53) Zeng, G.; Liu, Q.; Gu, R.; Zang, L.; Li, Y. *Catal. Today* **2011**, *178*, 206−213.
(54) Grasa, G. S.; Abanades, J. C. *Ind. Eng. Chem. Res.* **2006**, *45*, 8846−8851.
(55) Broda, M.; Müller, C. R. *Adv. Mater.* **2012**, *24*, 3059−3064.
(56) Kim, J. H.; Suh, D. J.; Park, T. J.; Kim, K. L. *Appl. Catal., A* **2000**, *197*, 191−200.
(57) Bartholomew, C. H.; Sorensen, W. L. *J. Catal.* **1983**, *81*, 131−141.
(58) Kuo, H. K.; Ganesan, P.; de Angelis, R. J. *J. Catal.* **1980**, *64*, 303−319.
(59) Bridge, G. W.; Chinchen, B. A. In *Catalyst Handbook*; ICI/Wolfe Scientific Books: London, 1970, pp 64−96.
(60) Borgars, D. J. Advances in Ammonia Plant Technology. In *Synthesis of Ammonia*; Vancini, V. A., Ed.; Macmillan: London, 1971; Chapter 10; p 261.
(61) Dennis, J. S.; Pacciani, R. *Chem. Eng. Sci.* **2009**, *64*, 2147−2157.
(62) Alvarez, D.; Abanades, J. C. *Ind. Eng. Chem. Res.* **2005**, *44*, 5608−5615.
(63) Borgwardt, R. H. *Chem. Eng. Sci.* **1989**, *44*, 53−60.
(64) Abanades, J. C.; Alvarez, D. *Energy Fuels* **2003**, *17*, 308−315.
(65) Pacciani, R.; Müller, C. R.; Davidson, J. F.; Dennis, J. S.; Hayhurst, A. N. *Can. J. Chem. Eng.* **2008**, *86*, 356−366.
(66) Li, L.; King, D. L.; Nie, Z.; Li, X. S.; Howard, C. *Energy Fuels* **2010**, *24*, 3698−3703.
(67) Lu, H.; Khan, A.; Pratsinis, S. E.; Smirniotis, P. G. *Energy Fuels* **2009**, *23*, 1093−1100.
(68) Hughes, R. W.; Lu, D.; Anthony, E. J.; Wu, Y. *Ind. Eng. Chem. Res.* **2004**, *43*, 5529−5539.
(69) Takenaka, S.; Ogihara, H.; Otsuka, K. *J. Catal.* **2002**, *208*, 54−63.
(70) Chen, D.; Christensen, K. O.; Ochoa-Fernandez, E.; Yu, Z.; Totdal, B.; Latoore, N.; Manzon, A.; Holmen, A. *J. Catal.* **2005**, *229*, 82−96.
(71) Zhang, Z.; Verykios, X. E.; MacDonald, S. M.; Affrossman, S. *J. Phys. Chem.* **1996**, *100*, 744−754.
(72) Guo, J.; Lou, H.; Zheng, X. *Carbon* **2007**, *45*, 1314−1321.
(73) Tang, S. B.; Qiu, F. L.; Lu, S. J. *Catal. Today* **1995**, *24*, 253−255.
(74) Chang, J. S.; Park, S. E.; Yoo, J. W.; Park, J. N *J. Catal.* **2000**, *195*, 1−11.
(75) Slagtern, A.; Schuurman, Y.; Leclercq, C.; Verykios, X.; Mirodatos, C. *J. Catal.* **1997**, *172*, 118−126.